High-throughput characterization of 309 photocrosslinker-bearing ASIC1a variants maps residues critical for channel function and pharmacology

Nina Braun[1], Søren Friis[2], Christian Ihling[3], Andrea Sinz[3], Jacob Andersen[1,#], Stephan A. Pless[1*]

[1]Department of Drug Design and Pharmacology, University of Copenhagen, Copenhagen, Denmark

[2]Nanion Technologies GmbH, Munich, Germany

[3]Department of Pharmaceutical Chemistry & Bioanalytics, Institute of Pharmacy, Charles Tanford Protein Center, Martin Luther University Halle-Wittenberg, Halle (Saale), Germany

[#]Current address: Lundbeck Research, H. Lundbeck A/S, Valby, Denmark

Short title: High-throughput analysis of ion channels containing non-canonical amino acids

* Corresponding Author:

Stephan A. Pless: stephan.pless@sund.ku.dk

Abstract

Incorporation of non-canonical amino acids (ncAAs) can endow proteins with novel functionalities, such as crosslinking or fluorescence. In ion channels, the function of these variants can be studied with great precision using standard electrophysiology, but this approach is typically labor intensive and low throughput. Here, we establish a high-throughput protocol to conduct functional and pharmacological investigations of ncAA-containing hASIC1a (human acid-sensing ion channel 1a) variants in transiently transfected mammalian cells. We introduce three different photocrosslinking ncAAs into 103 positions and assess the function of the resulting 309 variants with automated patch-clamp (APC). We demonstrate that the approach is efficient and versatile, as it is amenable to assessing even complex pharmacological modulation by peptides. The data show that the acidic pocket is a major determinant for current decay and live-cell crosslinking provides insight into the hASIC1a-psalmotoxin-1 interaction. Overall, this protocol will enable future APC-based studies of ncAA-containing ion channels in mammalian cells.

Introduction

Genetic code expansion approaches allow the incorporation of non-canonical amino acids (ncAAs) with unique chemical properties into proteins. Over the past two decades, this method has greatly facilitated protein modification and functionalization beyond the confines of the genetic code [1]. Ion channels have proven highly suited to ncAA incorporation, as evidenced by the success in introducing photocrosslinking, photoswitchable or fluorescent ncAAs into numerous members of this large and diverse protein family [2-4]. Among the ncAA subclasses, photocrosslinkers have proven particularly versatile, as they allow for the trapping of ion channels in certain conformational states [5-8], capturing of protein-protein interactions [9-12] and covalent linking of receptor-ligand complexes to delineate ligand binding sites [13-17].

Typically, incorporation of ncAAs is achieved by repurposing a stop codon to encode for a ncAA supplied by an orthogonal tRNA/aminoacyl tRNA synthetase (aaRS) pair. But the incorporation efficiency can be variable and unspecific incorporation of naturally occurring amino acids can result in inhomogeneous protein populations [2]. Verification of site-specific ncAA incorporation can therefore be laborious and time-consuming, especially in combination with detailed functional characterization. As a result, most studies have focused on only a limited number of incorporation sites, and the evaluation of potential functional or pharmacological effects of ncAA incorporation often remained minimal. In principle, automated patch-clamp (APC) devices offer fast and efficient high-throughput testing and have recently gained increasing popularity for electrophysiological interrogation of a diverse set of ion channels [18-22]. However, a combination of low efficiency of transient transfection in mammalian cells and limited ncAA incorporation rates have thus far prevented functional screening of ncAA-containing ion channel variants on APC platforms.

Here, we sought to overcome these limitations by developing a fluorescence-activated cell sorting (FACS)-based approach to enrich the population of transiently transfected cells expressing ncAA-containing ion channels. Using the human acid-sensing ion channel 1a (hASIC1a) as an example, we incorporated three different ncAA photocrosslinkers (AzF (4-Azido-L-phenylalanine), Bpa (4-Benzoyl-L-phenylalanine) and Se-AbK ((R)-2-Amino-3-{2-[2-(3-methyl-3H-diazirin-3-yl)-

ethoxycarbonylamino]-ethylselanyl}-propionic acid)) at 103 positions throughout its intracellular, extracellular and transmembrane domains.

ASICs are trimeric ligand-gated ion channels that open a weakly sodium-selective pore in response to proton binding to the so-called acidic pocket and likely other sites in the extracellular domain [23]. Apart from contributions to synaptic plasticity [24, 25], ASICs have recently gained increasing attention as potential drug targets for pain and stroke [26-35]. The six different human ASIC isoforms (ASIC1a, 1b, 2a, 2b, 3 and 4) are modulated by an impressive array of neuropeptides and venom-derived toxins that bind to the large extracellular domain [24, 36, 37]. Intriguingly, the extent and type of modulation (e.g. inhibition vs potentiation) are often highly dependent on ambient proton concentration, as well as subtype and species origin [38, 39]. This poses challenges for pharmacological profiling and motivates a detailed understanding of the mechanism and site of action of these peptides, to eventually generate lead compounds that could potentially target pain or stroke.

In this study, we establish a protocol to functionally screen ncAA-containing ion channels in transiently transfected cells on an APC platform. The 384-well setup of the SyncroPatch 384PE (Nanion Technologies) allows the efficient characterization of 309 hASIC1a variants and we show that ncAA incorporation is tolerated in over 50% of the positions. Incorporation of bulky ncAA photocrosslinkers generally results in lower pH sensitivity, especially around the acidic pocket, where ncAA incorporation also greatly accelerates current decay kinetics. We further demonstrate differential channel modulation by the neuropeptide big dynorphin (BigDyn; [40]) and by psalmotoxin-1 (PcTx1; [41]), a toxin derived from tarantula venom. Lastly, we turn to UV-induced photocrosslinking to covalently trap channel-toxin complexes and thus map the hASIC1a-PcTx1 interaction in live cells. Overall, our work highlights that ncAA-containing ion channels are amenable to APC-based high-throughput screening. We further demonstrate how this approach, when used with ncAA photocrosslinkers, can be harnessed to investigate protein-peptide or protein-protein interactions *in cellulo*.

Results

Development of an APC screen to validate ncAA incorporation into hASIC1a

In order to efficiently assess functional incorporation of ncAAs into human ASIC1a (hASIC1a), we developed an APC screen to record proton-gated channel activation (Figure 1). To this end, we co-transfected 103 different hASIC1a variants containing individual TAG stop codons throughout the protein together with the suppressor tRNA/ncAA-RS pair for either AzF, Bpa or Se-AbK and a GFP-reporter carrying a TAG at Y40 (for Bpa and Se-AbK) or Y151 (for AzF) into custom-made ASIC1a-KO HEK 293T cells [17, 42-44]. The corresponding ncAA was supplied in the cell culture medium six hours after transfection or omitted from the experiment in incorporation control samples. To increase cell viability and uptake efficiency, we synthesized the methylester derivates of AzF and Bpa [8, 45]. This allowed us to supplement the cell media with 50- and 100-fold lower ncAA concentration compared to previous studies, respectively [7, 13]. After 48 hours, cells grown in the presence of ncAA were sorted for green fluorescence to enrich the population of transfected cells, which were then submitted to APC to record proton-gated currents. Using GFP fluorescence as a proxy, we determined a transfection efficiency of 62.9 ± 9.5% for hASIC1a WT and an average of 11.2 ± 5% for the ncAA variants (Table S1). Without the FACS step, the latter rate would translate into less than 10% of the APC wells being occupied by transfected cells, precluding efficient APC experiments. By contrast, the cell sorting improves occupation to around 65% of wells with successful patch also displaying proton-gated currents (63% for AzF, 69% for Bpa and 60% for Se-AbK) and is therefore an indispensable element for the use of transiently transfected cells in APC.

The 384-well system of the SyncroPatch 384PE allows for parallel concentration response curve measurements on hASIC1a WT and 11 different channel variants with untransfected and incorporation controls in less than one hour. Specifically, we embarked to functionally interrogate 103 positions throughout the hASIC1a sequence: 38 positions in the N-terminal domain (Figure S1), 24 positions in the transmembrane domain and interface region (Figure S2), 29 positions in the C-terminal domain (Figure S3) and 12 positions around the acidic pocket (Figure 3 and S6). The current traces in Figure 2A show typical pH-induced inward currents of hASIC1a WT with a pH_{50} of 6.64 ± 0.12 (n=182), in line with previous studies [46, 47], as well as a variant with lower proton

127 sensitivity containing AzF in the acidic pocket (T236AzF, pH_{50} 6.17 ± 0.14, n=10). Interestingly, the
128 incorporation of Bpa, AzF and Se-AbK at position W46 did not result in proton-gated currents (Figure
129 2A, Figure S2), despite a previous report showing functional incorporation of a bulky ncAA at this
130 conserved Trp in the M1 helix [48]. We analysed all variants for mean peak current size and pH_{50} to
131 compare incorporation efficiency and proton sensitivity, respectively (Figures S1-3, Table S1).
132 Furthermore, we routinely assessed the extent of tachyphylaxis [49] and variants displaying >20%
133 current decrease after reaching the peak current are indicated in Figures 3 and S1-6 as well as Table
134 S1. To provide a comprehensive overview, we mapped incorporation patterns for the three
135 photocrosslinkers onto snake plots schematically depicting an ASIC1a subunit (Figure 2B-D). We
136 defined specific incorporation (circles with dark colour shade) as proton-gated currents of >1 nA
137 observed in the presence of ncAA, and minimal (<500 pA) proton-gated currents in the absence of
138 ncAA. If currents >1 nA were observed under both conditions, incorporation was considered
139 unspecific (circles with lighter colour shade), while positions labelled in grey did not yield substantial
140 currents in either condition (<1 nA). However, we cannot exclude the possibility of underestimating
141 the degree of unspecific incorporation, as enriching transfected cells grown in the absence of ncAA
142 by FACS was not feasible due to the low number of cells displaying GFP fluorescence (2.2 ± 1.7%).
143 As is apparent from the snake plots, we observed mostly robust incorporation in the N-terminus,
144 around the acidic pocket and the in proximal C-terminus. Indeed, among the 80 positions tested up
145 to and including L465, AzF resulted in functional channel variants in 61% of cases, compared to 50%
146 for Bpa and 44% for Se-AbK (Figure 2E).
147

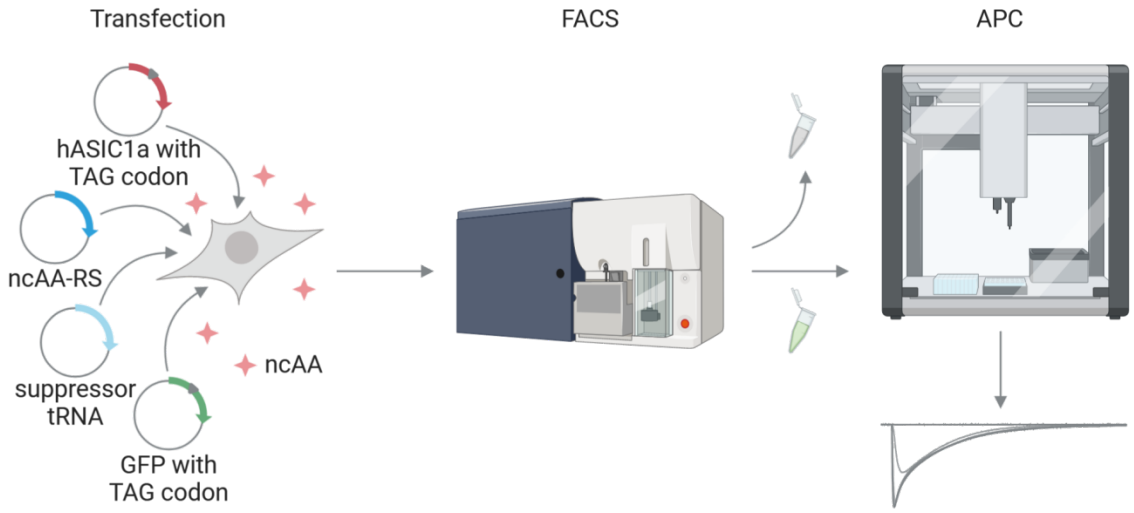

Figure 1: Schematic illustration of the workflow to assess ncAA incorporation into hASIC1a. HEK 293T ASIC1a-KO cells are transfected with hASIC1a containing a TAG stop codon at the site of interest, a co-evolved suppressor tRNA/ncAA-RS pair and a TAG-containing GFP reporter. ncAA is supplied in the cell culture medium. 48 hours after transfection, cells are sorted for green fluorescence on a FACS BD Aria I and those showing fluorescence are subjected to APC on a SyncroPatch 384PE to measure proton concentration response curves.

By contrast, all three crosslinkers showed mostly unspecific incorporation distal of L465, with WT-like current phenotypes from position 467 onwards (Figure S3 and S4A-C). This led us to hypothesize that channel constructs truncated in this region are functional. To investigate this further, we inserted an additional TGA stop codon for several variants, confirmed channel truncation by comparing molecular weight on a Western blot and measured concentration response curves in APC and two electrode voltage-clamp (TEVC) (Figure S4D-E). We found that channels truncated after H463 or K464 yielded no current in either APC or TEVC, but truncation after L465 produced a variant with strong tachyphylaxis in HEK 293T cells (Figure S4D) and truncation after C466 or R467 resulted in channels with WT-like proton sensitivity in both APC and TEVC. We conclude that the C-terminus distal of position 465 is not essential for proton-gated channel activity and that it is not possible to differentiate between currents originating from truncated and full-length protein to evaluate ncAA incorporation. We therefore added a C-terminal 1D4-tag to the hASIC1a construct to selectively purify full-length protein and compare the amounts in cells grown in the presence or absence of ncAA. This strategy confirms efficient incorporation in the distal C-terminus (Figure S5A).

Additionally, liquid chromatography/tandem mass spectrometry data revealed that Bpa can be specifically incorporated at positions distal of L465 (A480, Figure S5B).

For the 80 positions up to and including L465, we evaluated the incorporation efficiency of the ncAA photocrosslinkers based on the nature of the side chain occupying the position in the native channel and the position within the protein overall. We did not find evidence for pronounced global trends, but for instance Bpa incorporation was tolerated best at originally aromatic side chains (79%), while replacement of basic residues was least successful (27%) (Figure 2E). The three tested prolines could not be exchanged for any of the ncAAs. Interestingly, and in contrast to our expectations, Se-AbK incorporation only produced functional variants in 33% of cases when replacing structurally similar Lys and Arg side chains, while success rates were higher at polar and acidic side chains (58% and 54%, respectively). AzF incorporation rates were similar throughout all protein domains, whereas Bpa was better tolerated in the transmembrane regions and less in the N- and C-termini and Se-AbK incorporation in the M2 helix and C-terminus was negligible (Figure 2E). Overall, incorporating the three photocrosslinkers produced functional variants in all protein domains, albeit with varying success rates.

Together, we show that combining FACS with APC affords the time-efficient functional characterization of over 300 hASIC1a variants and provides a versatile platform to assess successful ncAA incorporation throughout all protein domains.

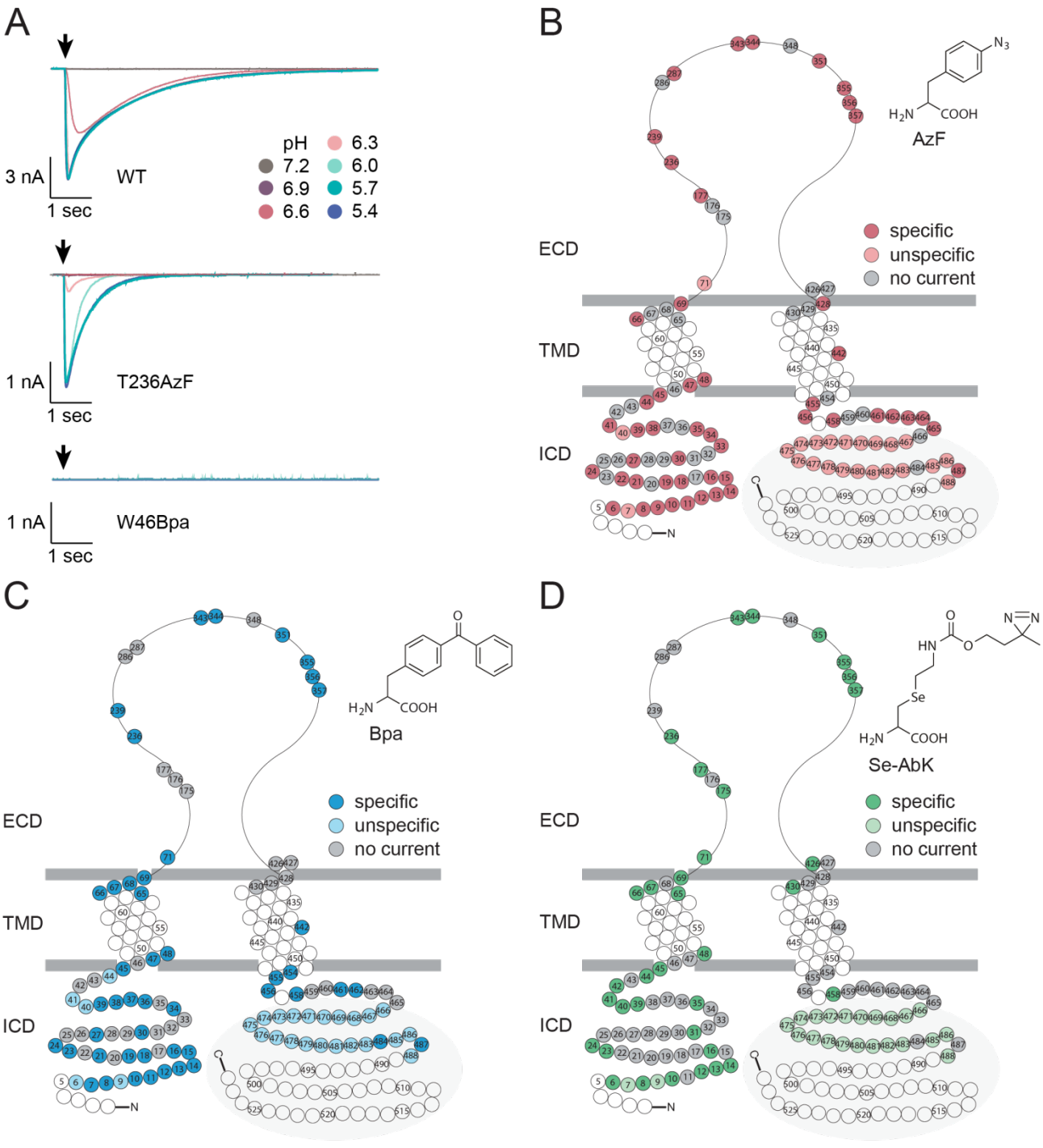

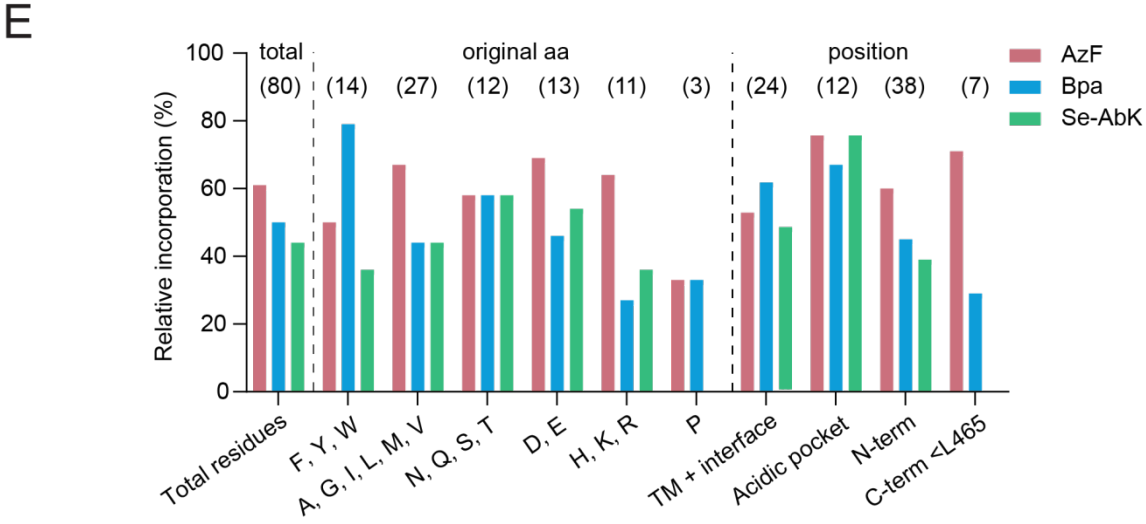

188

Figure 2: Incorporation of ncAA crosslinkers is tolerated in all domains of hASIC1a and produces functional channel variants. (A) Representative current traces for pH response curves of hASIC1a WT, T236AzF and W46Bpa recorded on the SyncroPatch 384PE. (B-D) Snake plot representations indicating specific, unspecific and unsuccessful incorporation (no current) for AzF (B), Bpa (C) and Se-AbK (D). Specific incorporation (circles with darker shade) is defined as pH-dependent peak currents >1 nA observed in cells grown in the presence, but not in the absence of ncAA, whereas unspecific incorporation (circles with lighter shade) indicates that currents were observed both in the presence and absence of ncAA. Positions indicated by grey circles did not yield functional channel variants when replaced by an ncAA (no current), while those coloured in white were not tested. The grey area highlights positions distal of L465. (E) Relative incorporation rates of AzF (red), Bpa (blue) and Se-AbK (green) at 80 different hASIC1a positions. Exchanged amino acids are grouped for original side chain properties and position within the channel, respectively (TM: transmembrane helices; N-term: N-terminus; C-term <L465: C-terminus up to and including L465). Positions distal of L465 were excluded from the analysis (highlighted in grey in B-D), as more distal deletions result in truncated, but functional channels (see Figures S3+4).

Photocrosslinker incorporation in the acidic pocket decreases proton sensitivity and accelerates current decay

During the design of the construct library for the APC screen, we consulted the 2.8 Å resolution structure of PcTx1 bound to chicken ASIC1 (PDB 4FZ0) to select 12 positions around the acidic pocket that are in sufficiently close proximity to potentially form covalent crosslinks with PcTx1 if replaced by a ncAA [50] (Figure S6A). Most of the resulting ncAA channel variants were functional, but in several instances, the initially applied proton concentration range of up to pH 5.4 did not yield saturating currents (Figure S6B/C). Consequently, we re-evaluated these variants using a lower pH range to resolve the pH_{50} and re-assess peak current size (Figure 3). This allowed us to determine EC_{50} values for all variants and confirmed that hASIC1a variants containing ncAAs in the acidic pocket display markedly reduced proton sensitivity, with pH_{50} values as low as 5.49 ± 0.13 (T239Bpa, mean ± S.D., n=6) and 5.66 ± 0.26 (D357AzF, mean ± S.D., n=10). Additionally, we observed substantial changes in current shape compared to WT. For example, T239Bpa and D357AzF showed dramatically increased current decay rates compared to WT, indicating possible effects of the photocrosslinkers on channel gating (rates of desensitization or closure). Overall, we found that incorporation of Se-AbK was least efficient, so all subsequent experiments focused on AzF- and Bpa-containing channel variants.

As hASIC1a variants with ncAAs around the acidic pocket displayed markedly altered proton sensitivity and current decay rates, we next wanted to assess if these variants can still be modulated by two peptide gating modifiers that interact with the acidic pocket, BigDyn and PcTx1.

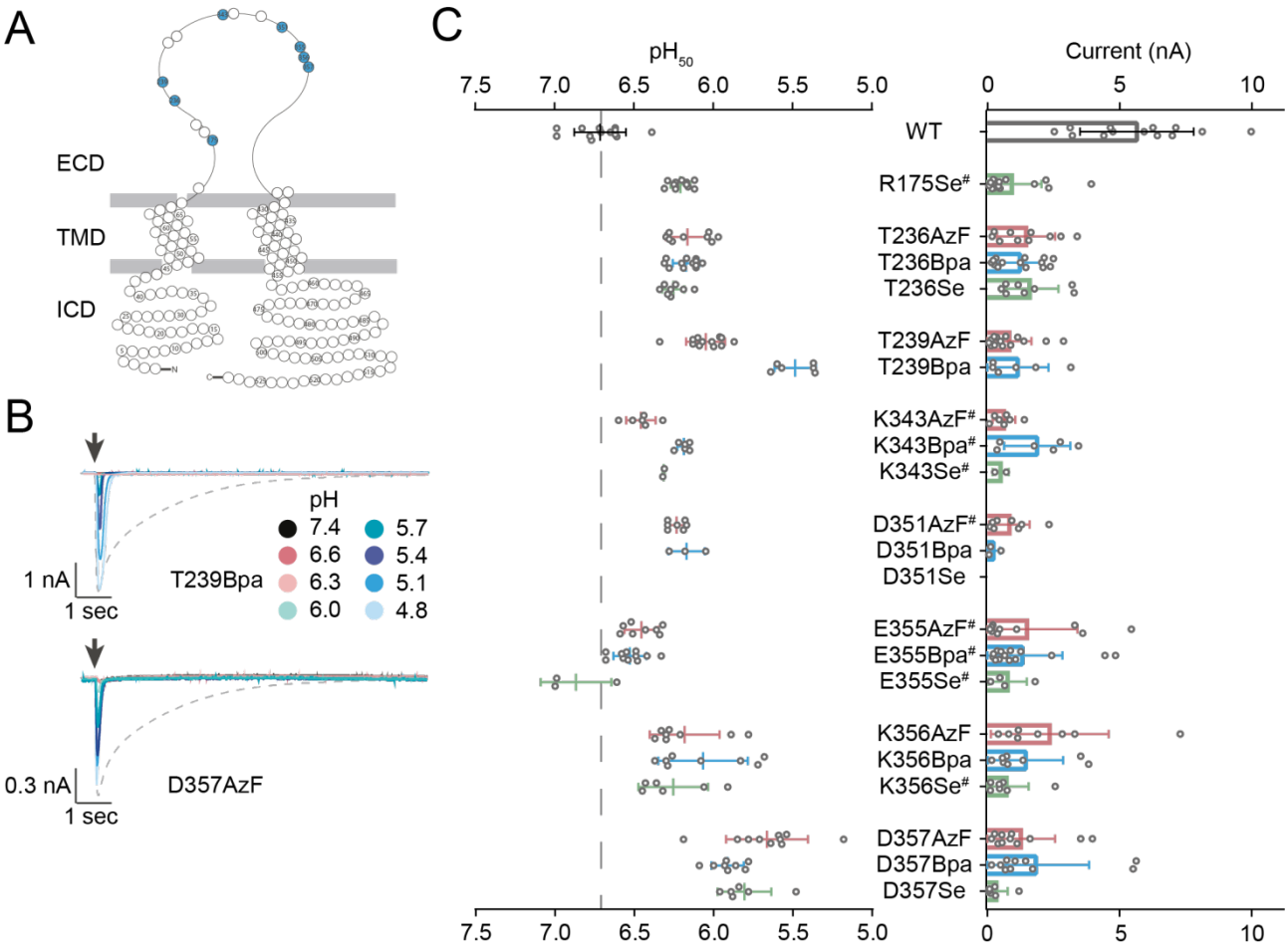

Figure 3: Incorporation of ncAA photocrosslinkers into the acidic pocket results in channel variants with lowered proton sensitivity and accelerated current decay. (A) Snake plot of hASIC1a with the assessed positions highlighted in blue. (B) Representative current traces of variants T239Bpa and D357AzF as recorded on the SyncroPatch 384PE, with arrows indicating the time of proton application. Dashed lines indicate WT current in response to pH 6.0 application. (C) Incorporation of AzF (red), Bpa (blue) and Se-AbK (green) at 8 positions around the acidic pocket results in lowered proton sensitivity for several variants. Dot plots comparing pH_{50} (left) and peak current sizes (right), bars indicate mean ± S.D., (#) indicates >20% tachyphylaxis (see also Figure S6 and Table S1).

Peptide modulation is retained in hASIC1a variants containing photocrosslinkers in the acidic pocket

First, we investigated the neuropeptide BigDyn, which interacts with the acidic pocket and shifts the proton dependence of both activation and SSD [17]. A key physiological function of BigDyn is to limit

ASIC1a steady-state desensitization (SSD) [40]. In order to define the appropriate pH for BigDyn application on each variant, we first established an APC-based protocol to determine SSD curves. Due to the open-well system of the SyncroPatch 384PE, lowering the conditioning pH to assess SSD required multiple mixing steps, which we simulated on a pH meter to determine the apparent pH the cells are exposed to before each activation. Using this approach, we obtained a pH_{50} SSD of 6.82 ± 0.03 for hASIC1a WT (n=27), which is lower than the value reported in *Xenopus laevis* oocytes (pH_{50} SSD = 7.05 ± 0.01, Figure S7A+B). Notably, we also observed a more shallow Hill slope for WT compared to oocytes (n_H 2.89 ± 0.47 vs 9.45 ± 2.84), but not for any of the tested variants in the acidic pocket or interface region (Figure S7B-F, Table S2). SSD profiles of the ncAA-containing variants varied with pH_{50} SSD values ranging from 7.11 ± 0.01 (E355Bpa, n=7) to 6.73 ± 0.09 (K356AzF, n=3, Table S2), with most variants displaying a slightly increased proton sensitivity compared to WT. This is in contrast to the observed pattern of reduced proton sensitivity for proton-gated activation, suggesting that incorporation of ncAA photocrosslinkers in the acidic pocket modulates proton sensitivity of activation and SSD differentially. For our subsequent APC experiments to assess BigDyn modulation, we chose a conditioning pH that led to around 10% remaining current upon activation.

Here, we focused on AzF-containing variants for which we had previously detected crosslinking to BigDyn on Western blots to evaluate if the observed peptide-channel interaction also results in functional modulation [17]. Cells were exposed to SSD-inducing pH conditions in the presence or absence of 3 µM BigDyn and the resulting currents upon pH 5.6 activation were normalized to control currents after incubation at pH 7.6 (Figure 4A+B). Control cells not exposed to BigDyn exhibited SSD to 0-30% mean remaining current (Figure S8, Table S3), while BigDyn co-application during conditioning limited SSD to varying degrees (Figure 4B). BigDyn increased rescue from pH-induced SSD in WT and all tested AzF-containing variants, although the effect was only significant for E355AzF and K356AzF (Figure 4B). For all tested variants, we regularly observed incomplete SSD after the first conditioning step, but this typically increased after the second conditioning step (see Figure S8). This could point towards possible confounding effects by the repeated solution mixing to achieve the desired conditioning pH described above. However, despite the reduced control over the conditioning pH compared to using a perfusion system with continuous flow, it was still possible

to determine if BigDyn modulates hASIC1a SSD. In short, the APC setup enables rapid evaluation of several channel variants with different SSD profiles for BigDyn modulation in a single experiment.

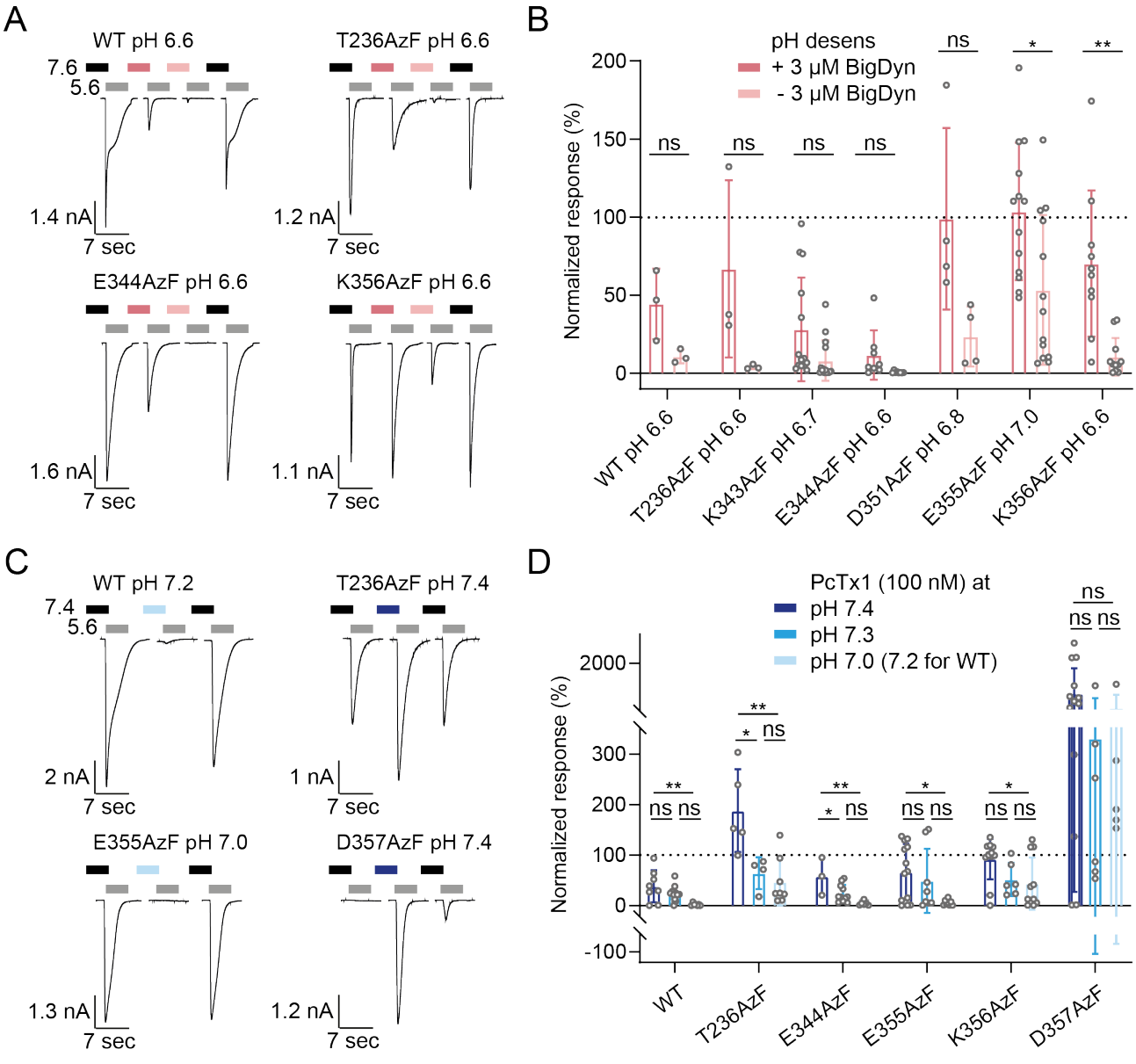

Figure 4: Peptide modulation of hASIC1a WT and selected variants containing AzF in the acidic pocket. (A) Characteristic current traces and (B) normalized response after SSD in absence or presence of BigDyn for hASIC1a WT and six ncAA variants. Cells were incubated at the desensitizing pH specified for each variant with or without 3 µM BigDyn for 2 min (pink bars) before activation at pH 5.6 (grey bars, 5 sec) and the currents were normalized to the average of two control currents after conditioning at pH 7.6 (black bars; control traces shown in Figure S8). (C) Exemplary current traces and (D) bar graph for PcTx1 modulation of hASIC1a WT and selected variants containing AzF in the acidic pocket at different pH. Cells were incubated with 100 nM PcTx1 at varying pH for 2 min (blue bars) before activation at pH 5.6 (grey bars, 5 sec) and the current was

normalized to the average of the four preceding and following control currents after conditioning at pH 7.4 (black bars). Bar graphs show mean ± S.D, dashed line indicates 100%, values in Table S3 and S4. (*) denotes significant difference between groups, $p < 0.05$; (**): $p < 0.01$; ns: not significant; student's t-test, unpaired with Welch's correction (B) or one-way ANOVA with Tukey's multiple comparisons test (D). Coloured and black bars in (A) and (C) not to scale.

We next tested a subset of AzF-containing acidic pocket variants for modulation by the gating modifier PcTx1, which was originally isolated from the venom of the *Psalmopoeus cambridgei* tarantula [41]. PcTx1 has previously been shown to increase the apparent proton affinity of both activation and steady-state desensitization of ASIC1a, resulting in inhibition or potentiation, depending on the application pH [39, 41, 51]. Here, we assessed hASIC1a modulation by co-applying 100 nM PcTx1 at varying conditioning pH and compared the resulting current upon activation with pH 5.6 to the average of the preceding and following control currents after conditioning at pH 7.4 (Figure 4C). For hASIC1a WT, we observed increasing inhibition from 38.15 ± 31.65% of current remaining at pH 7.4 to 2.06 ± 2.50% at pH 7.2 (Figure 4D, Table S4). This is in agreement with previous findings that the PcTx1 IC_{50} decreases at lower pH values [39]. Channel variants with AzF in positions 344, 355 or 356 showed a similar trend (Figure 4D). In contrast, we saw potentiation for T236AzF at pH 7.4 and for D357AzF at all tested proton concentrations (Figure 4C+D). This is consistent with the observation that these variants are among those with most pronounced reduction in the pH_{50} of activation (Figure 3 and S6, pH_{50} 6.17 ± 0.14 (n=10) and 5.66 ± 0.26 (n=10), respectively). D357AzF in particular exhibited an unusual phenotype: the first two control applications of pH 5.6 led to only very small or no detectable channel activation, but pH 5.6 after pre-application of the toxin induced a substantial inward current, after which the channels also activated in response to the following control applications.

Overall, the APC assay established here enabled the time-efficient characterization of pharmacological modulation of selected hASIC1a variants, providing an overview on their PcTx1 modulation profile at different application pH. Together, these results confirm that hASIC1a variants containing ncAA photocrosslinkers in the acidic pocket can still be modulated by known peptide gating modifiers, opening avenues to efficiently study peptide-channel interactions with a combination of APC and photocrosslinking.

Photocrosslinking confirms PcTx1 binding to the hASIC1a acidic pocket

Nine out of the originally targeted 12 positions around the PcTx1 binding site exhibited specific AzF incorporation (Figure 5A, left inset) and were used for photocrosslinking experiments followed by Western blotting following the workflow in Figure 5B. In parallel, six positions in the lower extracellular domain, F69, Y71, V80, D253, W287 and E413 were also replaced by AzF to confirm the specificity of potential photocrosslinking around the acidic pocket. (Figure 5A, right insets). hASIC1a variants were expressed in HEK293T ASIC-KO cells and 100 nM biotinylated PcTx1 was added before cells were exposed to UV light (365 nm) for 15 min to induce photocrosslinking. We then isolated full-length hASIC1a via a C-terminal 1D4-tag and analysed protein samples on a Western blot with antibodies against biotin and the 1D4-tag to detect PcTx1 and hASIC1a, respectively. Biotinylated PcTx1 was absent in UV-exposed hASIC1a WT and in all control positions containing AzF in the lower extracellular domain (F69, Y71, V80, D253, W287 and E413), as well as in samples containing AzF in the acidic pocket not exposed to UV light (Figure 5C). By contrast, PcTx1 was detected at four out of nine AzF-containing positions (344, 355, 356 and 357) after UV exposure, indicating covalent photocrosslinking at these positions (marked in red in Figure 5A), but at none of the five other sites in the acidic pocket tested (marked in green).

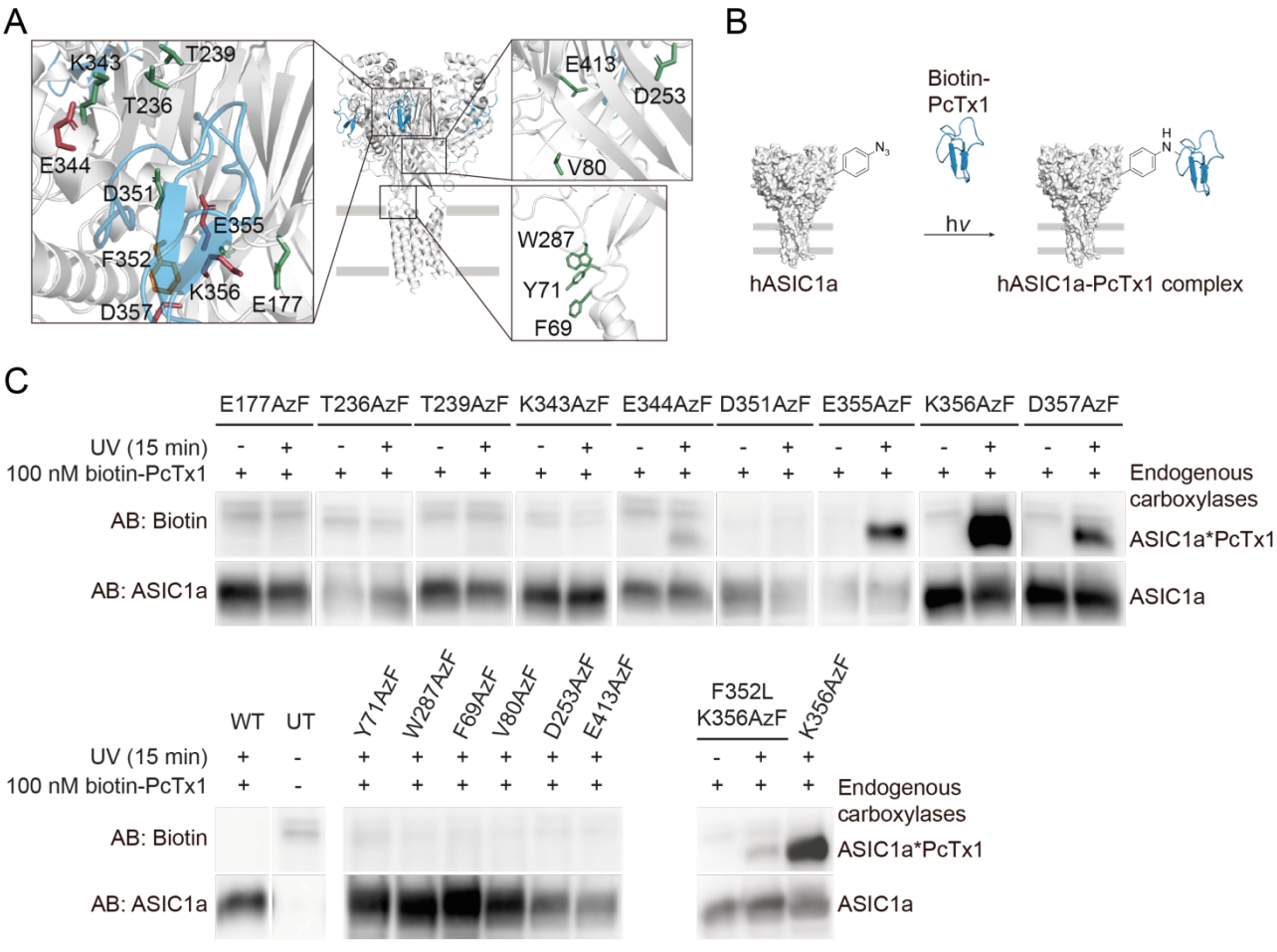

Figure 5: Live-cell photocrosslinking delineates the PcTx1 binding site at the ASIC1a acidic pocket. (A) Structure of cASIC1 (white) in complex with PcTx1 (blue, PDB: 4FZ0), insets show individual side chains replaced by AzF in the acidic pocket (left inset) and lower extracellular domain (right insets). Positions that crosslinked to biotin-PcTx1 are coloured red, F352 is marked in orange and positions that did not crosslink are coloured green. (B) Schematic workflow for crosslinking to biotin-PcTx1. HEK 293T ASIC1a-KO cells expressing AzF-containing hASIC1a variants are incubated with 100 nM biotin-PcTx1 and exposed to UV light for 15 min to form covalent hASIC1a-PcTx1 complexes, which are purified via a C-terminal 1D4-tag on hASIC1a and visualized via Western blotting. (C) Western blot of purified hASIC1a WT, untransfected cells (UT) and variants carrying AzF in the extracellular domain detected using the specified antibodies (AB). Biotin-PcTx1 is detected in UV-exposed samples containing AzF at positions 344, 355, 356 and 357 in the acidic pocket (coloured red in A, left inset), but not at positions 177, 236, 239, 343 or 351 (coloured green in A, left inset). PcTx1 is also absent in control samples not exposed to UV, those carrying AzF in the lower extracellular domain (right insets in A), WT or UTs. PcTx1 can be detected upon UV-exposing the toxin-insensitive F352L K356AzF double mutant (left inset in A, F352 coloured orange). Of note, the anti-biotin AB detects endogenous biotin-dependent carboxylases, which are also found in purified samples from UTs and have been described before [52, 53]. Data is representative of three individual experiments, see Figures S9-11 for original blots and crosslinking attempts with Bpa.

Previous studies have shown that the F352L mutation at the base of the acidic pocket eliminates the modulatory effect of PcTx1 on hASIC1a [54, 55], but it remained unclear if the toxin is still able to bind to hASIC1a. To test this possibility directly, we combined the F352L mutation with one of the crosslinking variants, resulting in the hASIC1a F352L K356AzF double mutant variant. Upon UV exposure, we were able to detect the PcTx1-hASIC1a complex even in the presence of the F352L mutation, albeit in lower amounts as assessed by the lower band intensity compared to the K356AzF single variant (Figure 5C, lower panel). This suggests that the F352L mutation does not eliminate toxin binding *per se*, but selectively abolishes the functional effects caused by PcTx1.

Attempts to photocrosslink PcTx1 using Bpa in the equivalent positions around the acidic pocket did not succeed (Figure S9). Yet overall, our photocrosslinking experiments confirm that PcTx1 interacts with the acidic pocket of hASIC1a, even in the presence of a mutation that abolishes the functional effects of PcTx1.

Discussion

First comprehensive functional assessment of ncAA-containing ion channels on an APC platform

Since their introduction, APC platforms have greatly aided ion channel research with their high throughput capabilities [56]. However, the requirement for high transfection rates to express the ion channels of interest limits the types of experiments that can be performed with this approach. Our FACS-assisted ncAA incorporation assay represents, to our knowledge, the first example of using an APC platform to functionally interrogate ncAA-containing ion channels. By transiently transfecting the protein of interest into mammalian cells and selecting those that express all components with FACS, we circumvent the need for stable cell lines. This method therefore greatly expands the scope of experiments that can be addressed using APC-based approaches.

Our extensive scanning of 309 ncAA-containing variants emphasizes the amenability of hASIC1a to ncAA incorporation, with the highest tolerance observed for AzF (61% functional variants) followed by Bpa (50%) and Se-AbK (44%) (Figure 2E). Previous studies on incorporation of AzF and Bpa into the human serotonin transporter (hSERT) and α-amino-3-hydroxy-5-methyl-4-isoxazolepropionic acid receptor (AMPAR) also show preferred functional incorporation of AzF and attribute this to its smaller size [7, 13]. Rannversson *et al*. report lowest ncAA tolerance in the hSERT TMD (44% and 20% for AzF and Bpa, respectively), contrasting our findings in the TM segments of hASIC1a (52% and 61%). However, it should be noted that we specifically selected the outer turns of the TM helices, where the study on AMPARs observed better incorporation compared to the more tightly packed central pore [7].

Previous work on hSERT shows higher success rates for replacing aromatic vs non-aromatic side chains, a trend we only observe for Bpa. Generally, genetic encoding of ncAAs does not appear to depend on the original properties of the replaced amino acid when assessed via protein expression [14, 57]. Indeed, a systematic examination of the effect of the similarly bulky ncAA acridonylalanine on protein solubility found no correlation to amino acid conservation, hydrophobicity or accessibility, but a close dependence on the location within the overall tertiary structure [58]. Consequently, the authors suggest that scientists broaden rather than narrow screens when aiming to introduce a ncAA into a new target protein. In the present study, we cover around 20% of hASIC1a and functionally

assess three different ncAAs, likely the most comprehensive investigation of genetic code expansion in a transmembrane protein to date.

Mechanistic insights into ASIC function

A beneficial side-effect of replacing native side chains with ncAA photocrosslinkers is that, in addition to their photoactivatable properties, these bulky side chains can also inform on basic biophysical aspects of the protein domain in question. Here, we show that incorporation of bulky, non-polar side chains leads to functional channels in about 50% of all cases, and we observe a general trend towards lower apparent proton affinity in the ncAA-bearing hASIC1a channels. This is particularly evident at positions in or near the acidic pocket, where previous studies have shown that mutations to acidic side chains in thumb and finger domains result in increased pH_{50} values (reviewed in [23]). By contrast, we only found a few positions in M1 (L45, Q66, F69) that resulted in higher apparent proton affinity. This is consistent with previous work on the nearby pre-M1 region [59], as well as a number of M1 and M2 mutations that mostly resulted in left-shifted pH_{50} values [48, 60]. Together, this suggests that mutations in M1 and M2 of ASIC1a have a general tendency to increase apparent proton affinity.

Generally, we observe that the time course of current decay is relatively heterogeneous (Figure 2 and 3, S6), likely due to the slow and incomplete solution exchange (see also below). This makes it difficult to quantify changes in for example activation or desensitization rates. Nevertheless, we observe that the same sites around the acidic pocket that show a pronounced decrease in apparent proton affinity also display a marked acceleration in current decay rates (Figure 3 and S6). This was consistently observed at all of the eight sites around the acidic pocket assessed in Figure 3 and was independent of the nature of the incorporated ncAA. This finding is coherent with a previous study that showed the thumb domain affects rates of fast desensitization [61]. Alternatively, it is conceivable that the observed phenotype is due to greatly increased channel deactivation rates [62]. Although we cannot discriminate between these possibilities, our data clearly show that the physico-chemical properties of side chains lining the acidic pocket are a major determinant for current decay in ASIC1a.

We also noticed varying degrees of tachyphylaxis, especially when positions in the external turns of the TM helices were replaced with ncAAs (Figure S2, Table S1). In light of previous work suggesting a contribution by permeating protons and an effect of hydrophobicity of TM1 side chains on tachyphylaxis, this warrants further investigation [49, 63].

Complex pharmacological modulation studied in ncAA-containing channels using APC

The complex pharmacological modulation pattern of hASIC1a by BigDyn and PcTx1 is notoriously challenging to study. However, we were able to optimize the APC protocols to replicate and even expand on the differential effects of this highly state-dependent peptide modulation (Figure 4). Specifically, we were able to show that despite the prominently lowered proton sensitivity of acidic pocket variants, all tested ncAA-containing hASIC1a variants retained some degree of modulation by both BigDyn and PcTx1. We observed varying degrees of BigDyn-dependent rescue from SSD for the different variants (Figure 4B). Under our conditions, rescue from SSD was incomplete when we applied 3 µM BigDyn, a concentration well above the reported EC_{50} range of 26-210 nM [17, 40]. In combination with the steep pH dependence of modulation, this resulted in considerable variability in the BigDyn modulation data, as evident by the reported range in S.D. values. While this can, at least in part, be attributed to our limited control over the BigDyn-application pH, we have made similar observations in a previous study using TEVC [17].

PcTx1 inhibited or potentiated AzF-containing hASIC1a variants in a pH dependent manner, in line with previous reports [39]. We examined a total of five variants, of which all except T236AzF also formed covalent complexes with the toxin upon UV exposure (Figure 5C). While PcTx1 still modulates and therefore interacts with hASIC1a T236AzF (Figure 4C+D), we cannot exclude that introduction of AzF at positions 177, 239, 343 or 351 prevents toxin interaction, as these variants were not assessed for PcTx1 modulation with APC and did not crosslink to the peptide upon UV exposure (Figure 5C).

Live-cell crosslinking provides a detailed map of the PcTx1-hASIC1a interaction

The acidic pocket is now well established both as a hotspot for channel activation and as a binding site for pharmacological modulators [17, 23]. In the case of PcTx1, structural data had already

444 outlined the toxin binding site on ASICs [50, 64], but unlike previous work, the crosslinking approach
445 outlined in this study enables us to covalently trap ligand-channel complexes in living cells. This
446 represents a notable advantage, especially for highly state-dependent interactions, such as those
447 between hASIC1a and BigDyn or PcTx1. Additionally, comparing the crosslinking pattern between
448 two ligands, the approach can indirectly inform on the varying degrees of conformational flexibility of
449 the ligands: BigDyn is likely to be highly flexible without a strong propensity to adopt a secondary
450 fold [65, 66], therefore samples a greater conformational space and is thus more likely to undergo
451 covalent crosslinking at multiple sites (9/9 sites tested at the acidic pocket, [17]). By contrast, PcTx1
452 folds into a compact and highly stable conformation and will consequently undergo covalent
453 crosslinking at relatively fewer sites (4/9 sites tested at the acidic pocket, Figure 5). These findings
454 also complement an earlier investigation of the key interactions between PcTx1 and ASIC1a that
455 concluded for the majority of contacts observed in the crystal structures to not persist during MD
456 simulations or to not be functionally relevant for PcTx1-mediated inhibition of ASIC1a [55].
457 The ability to covalently trap ligand-receptor complexes offers a unique opportunity to directly assess
458 if ASIC mutations shown to alter or abolish ligand effects still bind to the same site on the receptor.
459 For example, the hASIC1a F352L mutation at the base of the acidic pocket is known to almost
460 completely abolish the PcTx1-dependent modulation of ASIC1a channels [54, 55]. Yet it remained
461 unclear if the toxin also interacts with the acidic pocket in these mutant channels. Here, we directly
462 demonstrate that PcTx1 still binds to the acidic pocket, even at a concentration that is far too low to
463 have a functional effect on the mutant channels (100 nM). This leads us to propose that the F352L
464 mutation primarily affects conformational changes responsible for the PcTx1 effect on WT hASIC1a,
465 but not toxin binding *per se*.
466 We note that unlike AzF, we were unable to employ Bpa for crosslinking experiments with PcTx1.
467 We speculate that the introduction of this larger and more bulky photocrosslinker (compared to AzF)
468 partially occludes the acidic pocket and thus hinders binding of PcTx1. Alternatively, steric
469 constraints due to the positioning of the benzophenone diradical and the more selective reactivity of
470 Bpa (reacts exclusively with C-H bonds) may also play a role [67, 68]. Together, this emphasizes
471 that screens with multiple redundant ncAAs significantly increase chances of observing successful
472 crosslinking.

473

474 *Limitations of the outlined APC-based approach*

475 While our work establishes that ncAA-containing ion channels can be screened on an APC platform,
476 some limitations persist. Firstly, our present approach relies on simultaneous transfection of four
477 plasmids (Figure 1), which can negatively impact transfection efficiency and/or result in cells not
478 containing all four components. Careful optimization of DNA amounts and transfection conditions is
479 therefore necessary and a revised construct design to reduce the numbers of plasmids could further
480 improve yields. For example, the Plested group achieved co-expression of TAG-containing AMPAR
481 and GFP with an internal ribosome entry site (IRES) [5, 7], while Zhu and co-workers created a
482 bidirectional plasmid to encode both AzF-RS and tRNA [6]. This might be particularly fruitful for the
483 incorporation of Se-AbK, which was generally less efficient than that of AzF and Bpa (Figure 2E and
484 Table S1), despite others reporting robust incorporation of a similar ncAA [69].
485 Secondly, while GFP fluorescence indicates successful transfection and ncAA incorporation and
486 thereby increased likelihood of observing proton-gated currents in cells grown in the presence of
487 ncAA, it is not a reliable proxy for incorporation specificity in control cells grown in the absence of
488 ncAA. This is due to the fact that the degree of unspecific incorporation in GFP does not correlate
489 with that of the ncAA-containing hASIC1a variants. We consistently observed GFP fluorescence in
490 only around 2% of the control cells, independent of the co-expressed channel variant, which
491 translated to insufficient cell numbers for APC (requires a minimal concentration of 100.000 cells/ml).
492 Assuming that the transfection rates are similar in the presence and absence of ncAA (i.e. around
493 11%), we concluded that recording a larger number of unsorted control cells is the more stringent
494 approach to assess incorporation efficiency. We therefore did not subject the incorporation control
495 cells to FACS and instead conducted APC with the entire unsorted cell population.
496 Lastly, while APC platforms offer unprecedented throughput and speed, there are limitations with
497 regards to the rate and extent of perfusion exchange. This can be particularly challenging for ligand
498 application to fast-gating ligand-gated ion channels (i.e. pH changes for ASIC1a) in general and
499 strongly state-dependent pharmacological modulation (by e.g. BigDyn or PcTx1) in particular.
500 Although we were able to partially overcome these issues by employing a solution stacking
501 approach, we cannot draw detailed conclusions about activation or desensitization kinetics.

Similarly, values for proton-dependent activation and especially SSD can be determined with greater precision using TEVC or manual patch-clamp electrophysiology. However, note that the values reported here are generally in agreement with previous reports, both with regards to WT values [46, 47] and relative shifts caused by mutations, i.e. in the acidic pocket [23].

Conclusions and outlook

The ability to functionally screen ncAA-containing ion channels on APC platforms has the potential to greatly expand the use of ncAAs in both academic and industry settings. The intrinsically high throughput enables rapid assessment of incorporation efficiencies, functional properties and even complex pharmacological modulation. In principle, the approach can be used for both site-specific (this study) and global ncAA incorporation [70, 71], thus further increasing the number and type of chemical modifications that can be introduced. In the case of incorporation of photocrosslinking ncAAs, the approach can be exploited to crosslink to peptides (Figure 5, [17]), small molecules [13] or establish intra-protein crosslinking, including in protein complexes [8, 9]. Furthermore, the recently developed ability for on-chip optostimulation on related APC platforms [72] offers exciting prospects for potentially conducting UV-mediated crosslinking during live APC experiments in the future. Paired with MS and/or biochemical approaches [73, 74], the overall strategy could also be expanded to define interaction sites of unknown or known protein-protein interactions. Given that there are now well over 100 different ncAAs available for incorporation into proteins in mammalian cells [1, 75], the above approach will enable the efficient study of ion channels endowed with a wide range of properties or functionalities.

Material and Methods

Molecular biology. The complementary DNA (cDNA) encoding human ASIC1a (hASIC1a) was kindly provided by Dr. Stephan Kellenberger. Plasmids containing AzF-RS, Bpa-RS and tRNA were gifts from Dr. Thomas P. Sakmar [43]. AbK-RS and $tRNA_{pyl}$ in pcDNA3.1 were kindly provided by Professor Chris Ahern [44]. The dominant negative eukaryotic release factor (DN-eRF) was a gift from Dr. William Zagotta [76].

Site-directed mutagenesis was performed using PfuUltraII Fusion polymerase (Agilent, Denmark) and custom DNA mutagenesis primers (Eurofins Genomics, Germany). All sequences were confirmed by sequencing of the full coding frame (Eurofins Genomics). For hASIC1a constructs, a C-terminal 1D4-tag was added for protein purification and Western blot detection and two silent mutations were inserted at V10 and L30 to reduce the risk of potential reinitiation [77].

Cell culture and transfection. HEK 293T cells (ATCC®), in which endogenous hASIC1a was removed by CRISPR/Cas9 [17], were grown in monolayer in T75 or T175 flasks (Orange Scientific, Belgium) in DMEM (Gibco, Denmark) supplemented with 10 % FBS (Thermo Fisher Scientific, Denmark) and 1 % penicillin-streptomycin (Thermo Fisher Scientific) and incubated at 37 ˚C in a humidified 5 % CO_2 atmosphere. For APC experiments, cells were seeded into six-well plates (Orange Scientific) at a density of 300.000 cells/well and transfected the next day with Trans-IT LT1 (Mirus, WI, USA) and 1:1:1:1 µg DNA encoding hASIC1a TAG variants, ncAA-RS, tRNA and eGFP Y40TAG or Y151TAG, respectively. For the WT control, cells were transfected with 1 µg hASIC1a WT and 0.3 µg eGFP WT. Six hours after transfection, cell medium was replaced with supplemented DMEM containing 10 µM AzF- or Bpa-methylester (synthesis in SI) or 100 µM Se-AbK (custom-synthesized by ChiroBlock, Germany). FACS and APC recordings were performed 48 hours after transfection.

For crosslinking studies, cells were seeded into 15 cm dishes (VWR, Denmark) at a density of 5-7 mio. cells and transfected the next day with PEI (Polysciences, Germany) and 16:4:4:8 µg DNA encoding hASIC1a TAG variants, AzF-RS, tRNA and DN-eRF, respectively. For WT controls, 2 mio. cells were seeded into a 10 cm dish (VWR) and transfected with 8 µg hASIC1a WT. Six hours after transfection, cell medium was replaced with supplemented DMEM containing 0.5 mM AzF (Chem

552 Impex, IL, USA) or 1 mM Bpa (Bachem Bio, Switzerland) and crosslinking studies were performed
553 48 hours after transfection.
554
555 **FACS**. HEK 293T cells were washed with PBS, treated with Accutase (Sigma Aldrich, Denmark) or
556 Trypsin-EDTA (Thermo Fisher Scientific), pooled and centrifuged at 1000 rpm for 5 min. They were
557 resuspended in 350 µl of a 1:1 mixture of serum-free Hams F-12 nutrient mixture and extracellular
558 patch-clamp solution (140 mM NaCl, 4 mM KCl, 1 mM $MgCl_2$, 2 mM $CaCl_2$, 10 mM HEPES, pH 7.4)
559 supplemented with 20 mM HEPES and transported to the FACS core facility at ambient temperature.
560 A FACSAria I or III (BD Biosciences, CA, USA) with a 70 µm nozzle was used to sort cells for
561 singularity, size and GFP fluorescence (Excitation 488 nm, Emission 502 nm (low pass) and 530/30
562 nm (band pass)). Cells were filtered through a sterile 50 µm cup filcon (BD Biosciences) directly
563 before sorting to prevent clogging of the nozzle. The WT control was used to set the fluorescence
564 cutoff between GFP-positive and GFP-negative populations and to check the purity of the sort before
565 sorting 1 million GFP-positive cells for subsequent patch-clamp experiments. Where possible, a
566 minimum of 200000 GFP-positive cells were collected for hASIC1a TAG variants grown in presence
567 of ncAA, while controls grown in absence of ncAA and untransfected cells were not sorted. Cells
568 were collected in 1.5 ml tubes containing the 1:1 mixture mentioned above and transported to the
569 APC instrument at ambient temperature.
570
571 **Automated patch-clamp.** Automated whole-cell patch-clamp recordings were conducted on a
572 SyncroPatch 384PE (Nanion Technologies, Germany) directly after FACS sorting. Cells were loaded
573 into a teflon-coated plastic boat at concentrations of 1 million cells/ml (WT, controls grown in absence
574 of ncAA and untransfected cells) or 200000–400000 cells/ml (variants grown in presence of ncAA)
575 and incubated at 20 °C and 200 rpm. For patch-clamp recordings, a NPC®-384 medium resistance
576 single hole chip (Nanion Technologies) was filled with intracellular solution (120 mM KF, 20 mM KCl,
577 10 mM HEPES, pH 7.2) and extracellular solution (140 mM NaCl, 4 mM KCl, 1 mM $MgCl_2$, 2 mM
578 $CaCl_2$, 10 mM HEPES, pH 7.4). 30 µl of cells were loaded into each well and the cells were caught
579 on the holes by brief application of -200 mbar pressure and washed with 30 µl seal enhancer solution
580 (extracellular solution with 8 mM Ca^{2+}) under a holding pressure of -50 mbar. After a wash step with

extracellular solution, two more pulses of -200 mbar were applied to reach whole cell configuration and the cells were clamped at 0 mV under atmospheric pressure. For recordings of concentration-response curves, extracellular solutions at different pH were applied using a liquid stacking approach. Briefly, pipette tips were loaded with 45 µl of pH 7.4 wash solution followed by 5 µl of activating extracellular solution (pH 7.2-4.8). For each sweep, the baseline current was recorded for 1 sec before application of the 5 µl activating solution, while the pH 7.4 wash solution was dispensed with a delay of 5 sec to allow for recording of channel opening and desensitization in the presence of ligand. The second dispension was directly followed by aspiration of liquid and a second wash step with pH 7.4 before application of the next activating pH.

For SSD curve recordings, cells were exposed to an activating pH of 5.6 using the stacked addition protocol described above, while the conditioning pH was varied (pH 7.6-6.4). As the open-well system of the APC instrument does not allow a single exchange of the entire liquid surrounding the cell, the conditioning pH was adjusted stepwise by repeated addition and removal of solution. While this process was simulated at the pH meter to determine the apparent conditioning pH, small variations may occur due to mixing effects. At the end of each SSD curve recording, a control application of pH 5.6 after conditioning pH 7.6 was used to assess the extent of current rescue and exclude cells that did not recover from SSD.

For peptide modulation experiments, 0.1 % (w/v) bovine serum albumin (BSA, Sigma Aldrich) was added to the conditioning solutions to reduce peptide loss on boat and tip surfaces. To investigate modulation by BigDyn (synthesis described in [17]), cells were first exposed to two activations with pH 5.6 after conditioning at pH 7.6 to determine the control current, followed by two rounds of activation after 2 min conditioning with a pH that induces SSD and a control activation to evaluate current recovery. For half of the cell population, 3 µM BigDyn were co-applied during the second conditioning period to measure rescue from SSD. This assessment of SSD and recovery was repeated with peptide co-application during the first SSD-conditioning to also evaluate peptide wash out. To assess modulation by PcTx1 (Alomone labs, Israel, >95% purity), cells were exposed to two control measurements of activation with pH 5.6 after conditioning at pH 7.4, followed by pH 5.6 activation after incubation with 100 nM PcTx1 at varying pH (pH 7.4-7.0) for 2 min, as well as two further controls to assess recovery from modulation.

610

611 **Data analysis.** Current traces were acquired at 2 kHz and filtered in the DataControl384 software
612 using a Butterworth 4th order low pass filter at 45 Hz. Only cells with initial seals >100 MΩ were
613 considered for biophysical characterization using GraphPad Prism 7 or 8. This relatively low seal
614 cutoff in combination with the large proton-gated currents (up to 10 nA) recorded for WT and some
615 of the ncAA-containing variants resulted in suboptimal voltage-clamp conditions for a subpopulation
616 of cells, as also apparent from the current shapes. However, we have no evidence that this adversely
617 affected activation parameters or pharmacological modulation. Where possible, APC data was
618 pooled from a minimum of three cells and two separate recording days. On several occasions, an *n*
619 of five or more was acquired during the first screening trial, in which case the experiment was not
620 repeated. Current sizes were normalized to the respective control currents and half-maximal
621 concentrations (EC_{50} values) and Hill coefficients (n_H) calculated using equation (1). pH_{50} values
622 were calculated in Excel using equation (2). All values are expressed as mean ± S.D. (Standard
623 Deviation). The extent of tachyphylaxis for each recording was calculated by subtraction of the
624 normalized current at lowest pH from the normalized maximal current (> 20 % tachyphylaxis is
625 marked by ($^{\#}$)). Bar graphs and dot plots were made using GraphPad Prism 7 or 8 and SigmaPlot
626 13.0, while current traces were exported to Clampfit 10.5 and Adobe Illustrator CC 2019.

627 Equation (1): $$Y = \frac{100*\left(EC_{50}{}^{Hillslope}\right)}{\left(EC_{50}{}^{Hillslope}+\left(X^{Hillslope}\right)\right)}$$

628 Equation (2): $pH_{50}= -\log_{10}(EC_{50}[M])$

629 Mean current sizes and pH_{50} values of different cell lines and constructs were compared using
630 student's t-test or one-way ANOVA followed by Tukey's multiple comparisons test.

631

632 **Crosslinking studies, protein purification, western blotting**. Experiments were conducted as
633 described in [17], with two alterations: 1) Cell pellets were resuspended in 1 ml PBS (pH 7.4)
634 containing 100 nM biotinyl-PcTx1 (Phoenix Pharmaceuticals, CA, USA) and exposed to UV light for
635 15 min (AzF) or 60 min (Bpa), 2) Biotinyl-PcTx1 was detected using 1:1000 rabbit anti-biotin antibody
636 (abcam, UK) and 1:5000 goat anti-rabbit IgG HRP-conjugate (Promega, Denmak). Samples used
637 for incorporation controls were not exposed to UV light.

638

Funding

We acknowledge the Lundbeck Foundation (R139-2012-12390 to SAP and R218-2016-1490 to NB), the Boehringer Ingelheim Fond (to NB) and the University of Copenhagen for financial support.

Acknowledgements

We acknowledge the FACS core facility at the Biotech Research & Innovation Center (University of Copenhagen) for technical support. We thank Dr. Iacopo Galleano for the synthesis of AzF- and Bpa-ME, Dr. Christian Bernsen Borg for the synthesis of big dynorphin and members of the Pless laboratory for comments on the manuscript. Figure 1 was created with BioRender.com.

Competing interests

The authors declare no competing interests.

651

652 **References**

653 1. Chin JW. Expanding and reprogramming the genetic code. Nature. 2017;550(7674):53-60.
654 doi: 10.1038/nature24031. PubMed PMID: 28980641.
655 2. Braun N, Sheikh ZP, Pless SA. The current chemical biology tool box to study ion channels.
656 J Physiol. 2020. doi: 10.1113/JP276695. PubMed PMID: 32715480.
657 3. Paoletti P, Ellis-Davies GCR, Mourot A. Optical control of neuronal ion channels and
658 receptors. Nat Rev Neurosci. 2019. doi: 10.1038/s41583-019-0197-2. PubMed PMID: 31289380.
659 4. Klippenstein V, Mony L, Paoletti P. Probing Ion Channel Structure and Function Using Light-
660 Sensitive Amino Acids. Trends Biochem Sci. 2018;43(6):436-51. doi: 10.1016/j.tibs.2018.02.012.
661 PubMed PMID: 29650383.
662 5. Klippenstein V, Ghisi V, Wietstruk M, Plested AJ. Photoinactivation of glutamate receptors
663 by genetically encoded unnatural amino acids. J Neurosci. 2014;34(3):980-91. doi:
664 10.1523/JNEUROSCI.3725-13.2014. PubMed PMID: 24431456.
665 6. Zhu S, Riou M, Yao CA, Carvalho S, Rodriguez PC, Bensaude O, et al. Genetically encoding
666 a light switch in an ionotropic glutamate receptor reveals subunit-specific interfaces. Proc Natl Acad
667 Sci U S A. 2014;111(16):6081-6. doi: 10.1073/pnas.1318808111. PubMed PMID: 24715733;
668 PubMed Central PMCID: PMCPMC4000820.
669 7. Poulsen MH, Poshtiban A, Klippenstein V, Ghisi V, Plested AJR. Gating modules of the
670 AMPA receptor pore domain revealed by unnatural amino acid mutagenesis. Proc Natl Acad Sci U
671 S A. 2019;116(27):13358-67. doi: 10.1073/pnas.1818845116. PubMed PMID: 31213549; PubMed
672 Central PMCID: PMCPMC6613130.
673 8. Rook ML, Williamson A, Lueck JD, Musgaard M, Maclean DM. beta11-12 linker isomerization
674 governs acid-sensing ion channel desensitization and recovery. Elife. 2020;9. doi:
675 10.7554/eLife.51111. PubMed PMID: 32031522; PubMed Central PMCID: PMCPMC7041949.
676 9. Murray CI, Westhoff M, Eldstrom J, Thompson E, Emes R, Fedida D. Unnatural amino acid
677 photo-crosslinking of the IKs channel complex demonstrates a KCNE1:KCNQ1 stoichiometry of up

678 to 4:4. Elife. 2016;5. doi: 10.7554/eLife.11815. PubMed PMID: 26802629; PubMed Central PMCID:
679 PMCPMC4807126.
680 10. Westhoff M, Murray CI, Eldstrom J, Fedida D. Photo-Cross-Linking of IKs Demonstrates
681 State-Dependent Interactions between KCNE1 and KCNQ1. Biophys J. 2017;113(2):415-25. doi:
682 10.1016/j.bpj.2017.06.005. PubMed PMID: 28746852; PubMed Central PMCID: PMCPMC5529200.
683 11. Martin GM, Rex EA, Devaraneni P, Denton JS, Boodhansingh KE, DeLeon DD, et al.
684 Pharmacological Correction of Trafficking Defects in ATP-sensitive Potassium Channels Caused by
685 Sulfonylurea Receptor 1 Mutations. J Biol Chem. 2016;291(42):21971-83. doi:
686 10.1074/jbc.M116.749366. PubMed PMID: 27573238; PubMed Central PMCID: PMCPMC5063981.
687 12. Tian M, Ye S. Allosteric regulation in NMDA receptors revealed by the genetically encoded
688 photo-cross-linkers. Sci Rep. 2016;6:34751. doi: 10.1038/srep34751. PubMed PMID: 27713495;
689 PubMed Central PMCID: PMCPMC5054432.
690 13. Rannversson H, Andersen J, Sorensen L, Bang-Andersen B, Park M, Huber T, et al.
691 Genetically encoded photocrosslinkers locate the high-affinity binding site of antidepressant drugs
692 in the human serotonin transporter. Nat Commun. 2016;7:11261. doi: 10.1038/ncomms11261.
693 PubMed PMID: 27089947; PubMed Central PMCID: PMCPMC4838859.
694 14. Coin I, Katritch V, Sun T, Xiang Z, Siu FY, Beyermann M, et al. Genetically encoded chemical
695 probes in cells reveal the binding path of urocortin-I to CRF class B GPCR. Cell. 2013;155(6):1258-
696 69. doi: 10.1016/j.cell.2013.11.008. PubMed PMID: 24290358; PubMed Central PMCID:
697 PMC3916339.
698 15. Bottke T, Ernicke S, Serfling R, Ihling C, Burda E, Gurevich VV, et al. Exploring GPCR-
699 arrestin interfaces with genetically encoded crosslinkers. EMBO Rep. 2020:e50437. doi:
700 10.15252/embr.202050437. PubMed PMID: 32929862.
701 16. Reiners M, Margreiter MA, Oslender-Bujotzek A, Rossetti G, Grunder S, Schmidt A. The
702 Conorfamide RPRFa Stabilizes the Open Conformation of Acid-Sensing Ion Channel 3 via the
703 Nonproton Ligand-Sensing Domain. Mol Pharmacol. 2018;94(4):1114-24. doi:
704 10.1124/mol.118.112375. PubMed PMID: 30012583.
705 17. Borg CB, Braun N, Heusser SA, Bay Y, Weis D, Galleano I, et al. Mechanism and site of
706 action of big dynorphin on ASIC1a. Proc Natl Acad Sci U S A. 2020;117(13):7447-54. doi:

707 10.1073/pnas.1919323117. PubMed PMID: 32165542; PubMed Central PMCID:
708 PMCPMC7132280.
709 18. Kuenze G, Vanoye CG, Desai RR, Adusumilli S, Brewer KR, Woods H, et al. Allosteric
710 mechanism for KCNE1 modulation of KCNQ1 potassium channel activation. Elife. 2020;9. doi:
711 10.7554/eLife.57680. PubMed PMID: 33095155; PubMed Central PMCID: PMCPMC7584456.
712 19. Shen W, Ren W, Zhai S, Yang B, Vanoye CG, Mitra A, et al. Striatal Kir2 K+ channel inhibition
713 mediates the antidyskinetic effects of amantadine. J Clin Invest. 2020;130(5):2593-601. doi:
714 10.1172/JCI133398. PubMed PMID: 32310223; PubMed Central PMCID: PMCPMC7190977.
715 20. Silvera Ejneby M, Wallner B, Elinder F. Coupling stabilizers open KV1-type potassium
716 channels. Proc Natl Acad Sci U S A. 2020;117(43):27016-21. doi: 10.1073/pnas.2007965117.
717 PubMed PMID: 33051293; PubMed Central PMCID: PMCPMC7604479.
718 21. Xu H, Li T, Rohou A, Arthur CP, Tzakoniati F, Wong E, et al. Structural Basis of Nav1.7
719 Inhibition by a Gating-Modifier Spider Toxin. Cell. 2019;176(4):702-15 e14. doi:
720 10.1016/j.cell.2018.12.018. PubMed PMID: 30661758.
721 22. Chernov-Rogan T, Li T, Lu G, Verschoof H, Khakh K, Jones SW, et al. Mechanism-specific
722 assay design facilitates the discovery of Nav1.7-selective inhibitors. Proc Natl Acad Sci U S A.
723 2018;115(4):E792-E801. doi: 10.1073/pnas.1713701115. PubMed PMID: 29311306; PubMed
724 Central PMCID: PMCPMC5789920.
725 23. Rook ML, Musgaard M, MacLean DM. Coupling structure with function in acid-sensing ion
726 channels: challenges in pursuit of proton sensors. J Physiol. 2020. doi: 10.1113/JP278707. PubMed
727 PMID: 32306405.
728 24. Wemmie JA, Taugher RJ, Kreple CJ. Acid-sensing ion channels in pain and disease. Nat
729 Rev Neurosci. 2013;14(7):461-71. doi: 10.1038/nrn3529. PubMed PMID: 23783197; PubMed
730 Central PMCID: PMC4307015.
731 25. Vullo S, Kellenberger S. A molecular view of the function and pharmacology of acid-sensing
732 ion channels. Pharmacol Res. 2020;154:104166. doi: 10.1016/j.phrs.2019.02.005. PubMed PMID:
733 30731197.

734 26. Diochot S, Baron A, Salinas M, Douguet D, Scarzello S, Dabert-Gay AS, et al. Black mamba
735 venom peptides target acid-sensing ion channels to abolish pain. Nature. 2012;490(7421):552-5.
736 doi: 10.1038/nature11494. PubMed PMID: 23034652.
737 27. Verkest C, Piquet E, Diochot S, Dauvois M, Lanteri-Minet M, Lingueglia E, et al. Effects of
738 systemic inhibitors of acid-sensing ion channels 1 (ASIC1) against acute and chronic mechanical
739 allodynia in a rodent model of migraine. Br J Pharmacol. 2018;175(21):4154-66. doi:
740 10.1111/bph.14462. PubMed PMID: 30079481; PubMed Central PMCID: PMCPMC6177611.
741 28. Bohlen CJ, Chesler AT, Sharif-Naeini R, Medzihradszky KF, Zhou S, King D, et al. A
742 heteromeric Texas coral snake toxin targets acid-sensing ion channels to produce pain. Nature.
743 2011;479(7373):410-4. doi: 10.1038/nature10607. PubMed PMID: 22094702; PubMed Central
744 PMCID: PMC3226747.
745 29. Lee JYP, Saez NJ, Cristofori-Armstrong B, Anangi R, King GF, Smith MT, et al. Inhibition of
746 acid-sensing ion channels by diminazene and APETx2 evoke partial and highly variable
747 antihyperalgesia in a rat model of inflammatory pain. Br J Pharmacol. 2018;175(12):2204-18. Epub
748 2017/11/15. doi: 10.1111/bph.14089. PubMed PMID: 29134638; PubMed Central PMCID:
749 PMCPMC5980509.
750 30. Reimers C, Lee CH, Kalbacher H, Tian Y, Hung CH, Schmidt A, et al. Identification of a cono-
751 RFamide from the venom of Conus textile that targets ASIC3 and enhances muscle pain. Proc Natl
752 Acad Sci U S A. 2017;114(17):E3507-E15. Epub 2017/04/12. doi: 10.1073/pnas.1616232114.
753 PubMed PMID: 28396446; PubMed Central PMCID: PMCPMC5410773.
754 31. Xiong ZG, Zhu XM, Chu XP, Minami M, Hey J, Wei WL, et al. Neuroprotection in ischemia:
755 blocking calcium-permeable acid-sensing ion channels. Cell. 2004;118(6):687-98. Epub 2004/09/17.
756 doi: 10.1016/j.cell.2004.08.026. PubMed PMID: 15369669.
757 32. Wang YZ, Wang JJ, Huang Y, Liu F, Zeng WZ, Li Y, et al. Tissue acidosis induces neuronal
758 necroptosis via ASIC1a channel independent of its ionic conduction. Elife. 2015;4. doi:
759 10.7554/eLife.05682. PubMed PMID: 26523449; PubMed Central PMCID: PMCPMC4629285.
760 33. Wang JJ, Liu F, Yang F, Wang YZ, Qi X, Li Y, et al. Disruption of auto-inhibition underlies
761 conformational signaling of ASIC1a to induce neuronal necroptosis. Nat Commun. 2020;11(1):475.

762 doi: 10.1038/s41467-019-13873-0. PubMed PMID: 31980622; PubMed Central PMCID:
763 PMCPMC6981194.
764 34. Chassagnon IR, McCarthy CA, Chin YK, Pineda SS, Keramidas A, Mobli M, et al. Potent
765 neuroprotection after stroke afforded by a double-knot spider-venom peptide that inhibits acid-
766 sensing ion channel 1a. Proc Natl Acad Sci U S A. 2017;114(14):3750-5. Epub 2017/03/23. doi:
767 10.1073/pnas.1614728114. PubMed PMID: 28320941; PubMed Central PMCID:
768 PMCPMC5389327.
769 35. McCarthy CA, Rash LD, Chassagnon IR, King GF, Widdop RE. PcTx1 affords
770 neuroprotection in a conscious model of stroke in hypertensive rats via selective inhibition of ASIC1a.
771 Neuropharmacology. 2015;99:650-7. Epub 2015/09/01. doi: 10.1016/j.neuropharm.2015.08.040.
772 PubMed PMID: 26320544.
773 36. Rash LD. Acid-Sensing Ion Channel Pharmacology, Past, Present, and Future. Adv
774 Pharmacol. 2017;79:35-66. Epub 2017/05/23. doi: 10.1016/bs.apha.2017.02.001. PubMed PMID:
775 28528673.
776 37. Vyvers A, Schmidt A, Wiemuth D, Grunder S. Screening of 109 neuropeptides on ASICs
777 reveals no direct agonists and dynorphin A, YFMRFamide and endomorphin-1 as modulators. Sci
778 Rep. 2018;8(1):18000. doi: 10.1038/s41598-018-36125-5. PubMed PMID: 30573735; PubMed
779 Central PMCID: PMCPMC6301962.
780 38. Baron A, Diochot S, Salinas M, Deval E, Noel J, Lingueglia E. Venom toxins in the exploration
781 of molecular, physiological and pathophysiological functions of acid-sensing ion channels. Toxicon.
782 2013;75:187-204. Epub 2013/04/30. doi: 10.1016/j.toxicon.2013.04.008. PubMed PMID: 23624383.
783 39. Cristofori-Armstrong B, Saez NJ, Chassagnon IR, King GF, Rash LD. The modulation of acid-
784 sensing ion channel 1 by PcTx1 is pH-, subtype- and species-dependent: Importance of interactions
785 at the channel subunit interface and potential for engineering selective analogues. Biochem
786 Pharmacol. 2019;163:381-90. doi: 10.1016/j.bcp.2019.03.004. PubMed PMID: 30849303.
787 40. Sherwood TW, Askwith CC. Dynorphin opioid peptides enhance acid-sensing ion channel 1a
788 activity and acidosis-induced neuronal death. J Neurosci. 2009;29(45):14371-80. doi:
789 10.1523/JNEUROSCI.2186-09.2009. PubMed PMID: 19906984; PubMed Central PMCID:
790 PMC2802056.

791 41. Escoubas P, De Weille JR, Lecoq A, Diochot S, Waldmann R, Champigny G, et al. Isolation
792 of a tarantula toxin specific for a class of proton-gated Na+ channels. J Biol Chem.
793 2000;275(33):25116-21. doi: 10.1074/jbc.M003643200. PubMed PMID: 10829030.
794 42. Ye S, Kohrer C, Huber T, Kazmi M, Sachdev P, Yan EC, et al. Site-specific incorporation of
795 keto amino acids into functional G protein-coupled receptors using unnatural amino acid
796 mutagenesis. J Biol Chem. 2008;283(3):1525-33. doi: 10.1074/jbc.M707355200. PubMed PMID:
797 17993461.
798 43. Ye S, Huber T, Vogel R, Sakmar TP. FTIR analysis of GPCR activation using azido probes.
799 Nat Chem Biol. 2009;5(6):397-9. doi: 10.1038/nchembio.167. PubMed PMID: 19396177; PubMed
800 Central PMCID: PMCPMC2875874.
801 44. Chatterjee A, Xiao H, Bollong M, Ai HW, Schultz PG. Efficient viral delivery system for
802 unnatural amino acid mutagenesis in mammalian cells. P Natl Acad Sci USA. 2013;110(29):11803-
803 8. doi: 10.1073/pnas.1309584110. PubMed PMID: WOS:000322086100042.
804 45. Gordon SE, Munari M, Zagotta WN. Visualizing conformational dynamics of proteins in
805 solution and at the cell membrane. Elife. 2018;7. doi: 10.7554/eLife.37248. PubMed PMID:
806 29923827; PubMed Central PMCID: PMCPMC6056233.
807 46. Sherwood TW, Askwith CC. Endogenous arginine-phenylalanine-amide-related peptides
808 alter steady-state desensitization of ASIC1a. J Biol Chem. 2008;283(4):1818-30. Epub 2007/11/07.
809 doi: 10.1074/jbc.M705118200. PubMed PMID: 17984098.
810 47. Vaithia A, Vullo S, Peng Z, Alijevic O, Kellenberger S. Accelerated Current Decay Kinetics of
811 a Rare Human Acid-Sensing ion Channel 1a Variant That Is Used in Many Studies as Wild Type.
812 Front Mol Neurosci. 2019;12:133. doi: 10.3389/fnmol.2019.00133. PubMed PMID: 31178694;
813 PubMed Central PMCID: PMCPMC6542941.
814 48. Kasimova MA, Lynagh T, Sheikh ZP, Granata D, Borg CB, Carnevale V, et al. Evolutionarily
815 Conserved Interactions within the Pore Domain of Acid-Sensing Ion Channels. Biophys J.
816 2020;118(4):861-72. doi: 10.1016/j.bpj.2019.09.001. PubMed PMID: 31630811; PubMed Central
817 PMCID: PMCPMC7036722.
818 49. Chen X, Grunder S. Permeating protons contribute to tachyphylaxis of the acid-sensing ion
819 channel (ASIC) 1a. J Physiol. 2007;579(Pt 3):657-70. Epub 2007/01/06. doi:

820 10.1113/jphysiol.2006.120733. PubMed PMID: 17204502; PubMed Central PMCID:
821 PMCPMC2151377.
822 50. Baconguis I, Gouaux E. Structural plasticity and dynamic selectivity of acid-sensing ion
823 channel-spider toxin complexes. Nature. 2012;489(7416):400-5. Epub 2012/07/31. doi:
824 10.1038/nature11375. PubMed PMID: 22842900; PubMed Central PMCID: PMCPMC3725952.
825 51. Liu Y, Hagan R, Schoellerman J. Dual actions of Psalmotoxin at ASIC1a and ASIC2a
826 heteromeric channels (ASIC1a/2a). Sci Rep. 2018;8(1):7179. doi: 10.1038/s41598-018-25386-9.
827 PubMed PMID: 29739981; PubMed Central PMCID: PMCPMC5940917.
828 52. Ahmed R, Spikings E, Zhou S, Thompsett A, Zhang T. Pre-hybridisation: an efficient way of
829 suppressing endogenous biotin-binding activity inherent to biotin-streptavidin detection system. J
830 Immunol Methods. 2014;406:143-7. doi: 10.1016/j.jim.2014.03.010. PubMed PMID: 24657589.
831 53. Praul CA, Brubaker KD, Leach RM, Gay CV. Detection of endogenous biotin-containing
832 proteins in bone and cartilage cells with streptavidin systems. Biochem Biophys Res Commun.
833 1998;247(2):312-4. doi: 10.1006/bbrc.1998.8757. PubMed PMID: 9642122.
834 54. Sherwood T, Franke R, Conneely S, Joyner J, Arumugan P, Askwith C. Identification of
835 protein domains that control proton and calcium sensitivity of ASIC1a. J Biol Chem.
836 2009;284(41):27899-907. doi: 10.1074/jbc.M109.029009. PubMed PMID: 19654327; PubMed
837 Central PMCID: PMC2788841.
838 55. Saez NJ, Deplazes E, Cristofori-Armstrong B, Chassagnon IR, Lin X, Mobli M, et al.
839 Molecular dynamics and functional studies define a hot spot of crystal contacts essential for PcTx1
840 inhibition of acid-sensing ion channel 1a. Br J Pharmacol. 2015;172(20):4985-95. doi:
841 10.1111/bph.13267. PubMed PMID: 26248594; PubMed Central PMCID: PMC4621980.
842 56. Obergrussberger A, Friis S, Bruggemann A, Fertig N. Automated patch clamp in drug
843 discovery: major breakthroughs and innovation in the last decade. Expert Opin Drug Discov. 2020:1-
844 5. doi: 10.1080/17460441.2020.1791079. PubMed PMID: 32646308.
845 57. Ke YY, Huang YH, Chien WC, Loh HH, Chuang JY, Yeh SH. Mapping the naloxone binding
846 sites on the mu-opioid receptor using cell-based photocrosslinkers. Biochim Biophys Acta Proteins
847 Proteom. 2017;1865(3):336-43. doi: 10.1016/j.bbapap.2016.12.010. PubMed PMID: 28012872.

848 58. Hostetler ZM, Ferrie JJ, Bornstein MR, Sungwienwong I, Petersson EJ, Kohli RM. Systematic
849 Evaluation of Soluble Protein Expression Using a Fluorescent Unnatural Amino Acid Reveals No
850 Reliable Predictors of Tolerability. Acs Chemical Biology. 2018;13(10):2855-61. doi:
851 10.1021/acschembio.8b00696. PubMed PMID: WOS:000448488600005.
852 59. Coscoy S, de Weille JR, Lingueglia E, Lazdunski M. The pre-transmembrane 1 domain of
853 acid-sensing ion channels participates in the ion pore. J Biol Chem. 1999;274(15):10129-32.
854 PubMed PMID: 10187795.
855 60. Lynagh T, Flood E, Boiteux C, Wulf M, Komnatnyy VV, Colding JM, et al. A selectivity filter
856 at the intracellular end of the acid-sensing ion channel pore. Elife. 2017;6. Epub 2017/05/13. doi:
857 10.7554/eLife.24630. PubMed PMID: 28498103; PubMed Central PMCID: PMCPMC5449180.
858 61. Krauson AJ, Carattino MD. The Thumb Domain Mediates Acid-sensing Ion Channel
859 Desensitization. J Biol Chem. 2016;291(21):11407-19. doi: 10.1074/jbc.M115.702316. PubMed
860 PMID: 27015804; PubMed Central PMCID: PMCPMC4900284.
861 62. MacLean DM, Jayaraman V. Deactivation kinetics of acid-sensing ion channel 1a are strongly
862 pH-sensitive. Proc Natl Acad Sci U S A. 2017;114(12):E2504-E13. Epub 2017/03/08. doi:
863 10.1073/pnas.1620508114. PubMed PMID: 28265090; PubMed Central PMCID:
864 PMCPMC5373395.
865 63. Li T, Yang Y, Canessa CM. Impact of recovery from desensitization on acid-sensing ion
866 channel-1a (ASIC1a) current and response to high frequency stimulation. J Biol Chem.
867 2012;287(48):40680-9. Epub 2012/10/11. doi: 10.1074/jbc.M112.418400. PubMed PMID:
868 23048040; PubMed Central PMCID: PMCPMC3504781.
869 64. Dawson RJ, Benz J, Stohler P, Tetaz T, Joseph C, Huber S, et al. Structure of the acid-
870 sensing ion channel 1 in complex with the gating modifier Psalmotoxin 1. Nat Commun. 2012;3:936.
871 doi: 10.1038/ncomms1917. PubMed PMID: 22760635.
872 65. O'Connor C, White KL, Doncescu N, Didenko T, Roth BL, Czaplicki G, et al. NMR structure
873 and dynamics of the agonist dynorphin peptide bound to the human kappa opioid receptor. Proc Natl
874 Acad Sci U S A. 2015;112(38):11852-7. doi: 10.1073/pnas.1510117112. PubMed PMID: 26372966;
875 PubMed Central PMCID: PMCPMC4586840.

876 66. Ferre G, Czaplicki G, Demange P, Milon A. Structure and dynamics of dynorphin peptide and
877 its receptor. Vitam Horm. 2019;111:17-47. doi: 10.1016/bs.vh.2019.05.006. PubMed PMID:
878 31421700.
879 67. Grunbeck A, Huber T, Sachdev P, Sakmar TP. Mapping the ligand-binding site on a G
880 protein-coupled receptor (GPCR) using genetically encoded photocrosslinkers. Biochemistry.
881 2011;50(17):3411-3. doi: 10.1021/bi200214r. PubMed PMID: 21417335; PubMed Central PMCID:
882 PMCPMC3099303.
883 68. Dorman G, Prestwich GD. Benzophenone photophores in biochemistry. Biochemistry.
884 1994;33(19):5661-73. PubMed PMID: 8180191.
885 69. Ai HW, Shen W, Sagi A, Chen PR, Schultz PG. Probing protein-protein interactions with a
886 genetically encoded photo-crosslinking amino acid. Chembiochem. 2011;12(12):1854-7. doi:
887 10.1002/cbic.201100194. PubMed PMID: 21678540.
888 70. Gupta K, Toombes GE, Swartz KJ. Exploring structural dynamics of a membrane protein by
889 combining bioorthogonal chemistry and cysteine mutagenesis. Elife. 2019;8. doi:
890 10.7554/eLife.50776. PubMed PMID: 31714877; PubMed Central PMCID: PMCPMC6850778.
891 71. Piotrowski C, Ihling CH, Sinz A. Extending the cross-linking/mass spectrometry strategy:
892 Facile incorporation of photo-activatable amino acids into the model protein calmodulin in
893 Escherichia coli cells. Methods. 2015;89:121-7. doi: 10.1016/j.ymeth.2015.02.012. PubMed PMID:
894 25726908.
895 72. Boddum K, Skafte-Pedersen P, Rolland JF, Wilson S. Optogenetics and Optical Tools in
896 Automated Patch Clamping. Methods Mol Biol. 2021;2188:311-30. doi: 10.1007/978-1-0716-0818-
897 0_16. PubMed PMID: 33119859.
898 73. Hoffmann JE. Bifunctional Non-Canonical Amino Acids: Combining Photo-Crosslinking with
899 Click Chemistry. Biomolecules. 2020;10(4). doi: 10.3390/biom10040578. PubMed PMID: 32290035;
900 PubMed Central PMCID: PMCPMC7226127.
901 74. Wu X, Spence JS, Das T, Yuan X, Chen C, Zhang Y, et al. Site-Specific Photo-Crosslinking
902 Proteomics Reveal Regulation of IFITM3 Trafficking and Turnover by VCP/p97 ATPase. Cell Chem
903 Biol. 2020;27(5):571-85 e6. doi: 10.1016/j.chembiol.2020.03.004. PubMed PMID: 32243810;
904 PubMed Central PMCID: PMCPMC7194980.

905 75. Dumas A, Lercher L, Spicer CD, Davis BG. Designing logical codon reassignment -
906 Expanding the chemistry in biology. Chem Sci. 2015;6(1):50-69. doi: 10.1039/c4sc01534g. PubMed
907 PMID: 28553457; PubMed Central PMCID: PMCPMC5424465.
908 76. Schmied WH, Elsasser SJ, Uttamapinant C, Chin JW. Efficient multisite unnatural amino acid
909 incorporation in mammalian cells via optimized pyrrolysyl tRNA synthetase/tRNA expression and
910 engineered eRF1. J Am Chem Soc. 2014;136(44):15577-83. doi: 10.1021/ja5069728. PubMed
911 PMID: 25350841; PubMed Central PMCID: PMCPMC4333590.
912 77. Kalstrup T, Blunck R. Reinitiation at non-canonical start codons leads to leak expression
913 when incorporating unnatural amino acids. Scientific reports. 2015;5:11866. Epub 2015/07/15. doi:
914 10.1038/srep11866. PubMed PMID: 26153354; PubMed Central PMCID: PMCPMC4648390.

915